



**HAL**  
open science

# Assessment of 2D Digital Image Correlation for Experimental Modal Analysis of Transient Response of Beams Using a Continuous Wavelet Transform Method

Xavier Régal, Gwendal Cumunel, Michel Bornert, Marc Quiertant

► **To cite this version:**

Xavier Régal, Gwendal Cumunel, Michel Bornert, Marc Quiertant. Assessment of 2D Digital Image Correlation for Experimental Modal Analysis of Transient Response of Beams Using a Continuous Wavelet Transform Method. Applied Sciences, 2023, 13 (8), pp.4792. 10.3390/app13084792. hal-04067383

**HAL Id: hal-04067383**

**<https://hal.science/hal-04067383v1>**

Submitted on 13 Apr 2023

**HAL** is a multi-disciplinary open access archive for the deposit and dissemination of scientific research documents, whether they are published or not. The documents may come from teaching and research institutions in France or abroad, or from public or private research centers.

L'archive ouverte pluridisciplinaire **HAL**, est destinée au dépôt et à la diffusion de documents scientifiques de niveau recherche, publiés ou non, émanant des établissements d'enseignement et de recherche français ou étrangers, des laboratoires publics ou privés.



Distributed under a Creative Commons Attribution 4.0 International License

## Article

# Assessment of 2D Digital Image Correlation for Experimental Modal Analysis of Transient Response of Beams Using a Continuous Wavelet Transform Method

Xavier Régal <sup>1</sup>, Gwendal Cumunel <sup>1,\*</sup>, Michel Bornert <sup>1</sup> and Marc Quiertant <sup>2</sup>

<sup>1</sup> Lab Navier, Gustave Eiffel University, ENPC, CNRS, F-77455 Marne-la-Vallée, France; xavier.francois.regal@gmail.com (X.R.); michel.bornert@enpc.fr (M.B.)

<sup>2</sup> MAST, EMGCU, Gustave Eiffel University, F-77447 Marne-la-Vallée, France; marc.quiertant@univ-eiffel.fr

\* Correspondence: gwendal.cumunel@enpc.fr

**Abstract:** The modal parameters of structures, and in particular their mode shapes, are generally determined based on the measurement of accelerometers or laser vibrometers. However, these sensors do not allow the performance of full-field measurements. In this study, the free vibration of a beam triggered by a shock is investigated using a high-speed camera with high image definition. With the help of digital image correlation (DIC), the beam displacement fields are deduced from the images. To analyse the DIC measurement quality, different tests and analyses are performed. First, the systematic errors and uncertainties in the DIC calculation for a simple translation are analysed considering different speckles. Then, tests on two configurations of a vibrating beam are filmed and full-field displacement measurements are computed. The modal parameters of the beam are deduced from these measurements using a continuous wavelet transform method. Particular care was taken to adapt the method to the post-processing of the numerous and noisy signals obtained for these experiments. All the steps of the post-processing are detailed in this paper. Finally, the modal parameters obtained with the proposed method are compared with those obtained in a more classical way using accelerometers and from the beam theory. In particular, the comparison of the signal-to-noise ratio of the different measurement methods is discussed.

**Keywords:** structural vibration; experimental modal analysis; DIC; beam



**Citation:** Régal, X.; Cumunel, G.; Bornert, M.; Quiertant, M. Assessment of 2D Digital Image Correlation for Experimental Modal Analysis of Transient Response of Beams Using a Continuous Wavelet Transform Method. *Appl. Sci.* **2023**, *13*, 4792. <https://doi.org/10.3390/app13084792>

Academic Editor: Cecilia Surace

Received: 5 March 2023

Revised: 1 April 2023

Accepted: 5 April 2023

Published: 11 April 2023



**Copyright:** © 2023 by the authors. Licensee MDPI, Basel, Switzerland. This article is an open access article distributed under the terms and conditions of the Creative Commons Attribution (CC BY) license (<https://creativecommons.org/licenses/by/4.0/>).

## 1. Introduction

In order to identify the modal parameters of a structure it is necessary to deal with measurements such as acceleration, velocity, or displacement signals. These temporal signals can be processed, using the continuous wavelet transform for example, to determine the natural frequency, the damping ratio, and the mode shape for each mode. Nowadays, the current metrology tools for vibration measurement are mainly based on the use of accelerometers and laser vibrometers [1,2]. However, in order to obtain a sufficiently precise description of the mode shapes of a studied structure, a large number of sensors have to be installed. Depending on the size of the structure, the use of accelerometers can introduce additional damping due to the connecting cables, but also additional masses due to the sensors themselves [3]. The laser vibrometers require surfaces whose direction of reflection remains relatively unchanged during the test and free from edge effects. These conditions are difficult to guarantee in certain cases. In order to carry out field measurements (speed or displacement), scanning vibrometers also require the use of a periodic stationary excitation, which is a limitation.

For the past decade, digital image correlation (DIC) has been increasingly used in the mechanics of materials and structures to determine, in particular, 2D and 3D strain fields. Indeed, when the experimental conditions are optimal, it is possible to obtain a displacement resolution of less than one tenth or even one hundredth of a pixel [4]. This technique can

be applied for the analysis of dynamic loads with the use of high-speed cameras. However, the latter are often limited in terms of image definition, which restricts the spatial resolution of the analysis and penalizes the analysis of slender structures such as those encountered in civil engineering. New generations of cameras, presenting a wide variety of combinations of image definition and acquisition frequency, make it possible to push back these limits and thus constitute potential alternatives to the conventional modal analysis instrumentation.

In the literature, some studies have explored the use of fast imaging techniques to perform modal analysis of structural elements [5,6]. Bebernis et al. [7] have studied the influence of the speckle to identify the best suited for the monitoring of random vibration. Although there is a correlation between the size of the spots and the size of the patterns, this study does not take into account the size of the patterns used for the DIC, which are always  $15 \text{ px}^2$ . The different results obtained are compared with those inferred from strain gauges and laser vibrometer measurements. Although the application of imaging techniques in dynamic experiments is in constant progress, the studies of some authors, as in [8], are limited by the frame rate of the camera. Cameras with on-board memory (such as the Photron SA series) can reach higher frame rates, but their image definition is limited (typically 1 or 2 megapixels) and the test duration is then restricted by the available memory (a few seconds). Recent alternative camera technologies, associated with very high-speed data transfer solutions, permit us to record several thousand images per second at relatively high resolutions and during rather long sequences (e.g., 12 megapixels at 190 Hz for the JAI SP-12000M-CXP4, which can also be used at much higher frame rates on smaller images). More details will be given in the next part. The use of such a camera makes it possible to obtain a quasi-continuous measurement of the studied object. However, few tools have been developed to analyze this amount of information and most authors compare the displacement fields and the modal deformations obtained with the results of finite element (FE) calculations [9,10]. Some researchers caution about the frequency of cameras' fans, which can disturb the measurements [11,12]. In order to obtain the displacements using fast imaging, Chen et al. [13] have proposed a process called "video magnification", but the results obtained remain relatively noisy and inaccurate. It is clear from this preliminary overview that, despite several disadvantages, which are mainly the limited frame rate for high resolutions and the lower measurement accuracy with respect to strain gauges, DIC has several advantages in the field of vibratory analysis. Based on the above survey of the literature, this study investigates the transverse vibratory response of a beam excited by a shock with a focus on the analysis of the measurement quality (dispersion of the results, noise disturbance, random and systematic errors, uncertainty, etc.).

The first part of this paper describes the set-up used for the experimental study of the vibrating beam and briefly recalls the main principles of the DIC method. Particular attention is paid to the determination of the error and the uncertainty of the measured displacements [14] induced by the speckle characteristics (size of the spots and size of the patterns). Then, a fairly common modal identification based on the continuous wavelet transform method is presented; however, a signal processing procedure is proposed to deal with the numerous and noisy signals obtained from the DIC measurements. The standard deviation of the experimental results is also discussed and a process to remove the noise disturbance is presented. Next, the main experimental results are shown for two boundary conditions of the beam (clamped–clamped and clamped–free) and compared with results of a theoretical calculation and with data sets from accelerometers. Finally, concluding remarks are discussed.

## 2. Experimental Implementation of DIC

### 2.1. Experimental Set-Up

The structure chosen for carrying out an experimental modal analysis using DIC is an aluminum beam of width  $b = 30 \text{ mm}$  and thickness  $h = 6 \text{ mm}$ . The Young's modulus and the density of the beam were experimentally determined and are respectively equal to  $E = 71.8 \text{ GPa}$  and  $\rho = 2760 \text{ kg}\cdot\text{m}^{-3}$ . The boundary conditions are either clamped–clamped,

with length  $L = 505$  mm, or cantilever, with length  $L = 570$  mm. The beam is subjected to a shock produced with an instrumented impact hammer system. This system consists of a hammer head (Brüel & Kjær type 8200) mounted with a spring like a pinball plunger. In this way, double shocks are avoided and the impact duration can be adjusted. This kind of excitation leads to the solicitation of a maximum number of modes. Moreover, we are able to measure the excitation signal. In order to isolate, as much as possible, the experimental set-up from external disturbances, the latter one is mounted on a breadboard. The vibratory response of the beam is recorded using a JAI SP-12000M-CXP4 fast camera that directly records images within the RAM of the host computer. This camera, equipped with a macro lens from Zeiss (DISTAGON T 2/35 ZF-I), is set above the beam by means of a gantry mounted on the same breadboard at a distance such that the whole beam is observed within the width of the field of view. The frame rate of the image acquisition is limited by the internal data processing of the camera and the speed of the bus that transfers them to the host computer. At full definition ( $4096 \times 3072$  px<sup>2</sup>), it reaches 190 frames per second (fps). However, such a definition is useless for a slender structure such as our beam. An image definition of  $4096 \times 80$  px<sup>2</sup> is sufficient to image the whole system, with the same image resolution, and permits a much larger frame rate of 5439 fps. In order to avoid images being blurred by motion during the shooting, the integration time of the camera is set to its minimal value: 15  $\mu$ s. Therefore, sufficient light is required for the object to be imaged with the best signal-to-noise ratio of the camera. In our case, the beam was illuminated using four pulsed LED spots (developed by R&D Vision), which light the scene with pulses having a duration of 8  $\mu$ s, i.e., slightly more than half of the integration time. This system is synchronized with the camera using an external trigger box (EG, synchronization electronics developed by R&D Vision). For the chosen image resolution, this illumination system restrains the maximum fps we can choose for the camera since the maximum reachable light pulse frequency for the system is about 4500 Hz due to the cyclic pulse duration limit of the LED. The acquisition of the frames is therefore performed at this sampling frequency. This allows us to record sequences of typically 10 to 15 thousand images, from which displacement data need to be extracted.

In addition, ten accelerometers are installed on the beam in order to compare the results of the modal analysis performed using the DIC measurements with those obtained with such more conventional sensors. Data acquisition of the accelerometers and the force sensor is carried out using NI CompactDAQ equipment (housing 9174 with three modules 9234). For this system, the sampling frequency is chosen equal to 10,240 Hz so as, on one hand, to investigate the presence of other modes beyond the range of frequencies studied by the optical system [0–4500] Hz and, on the other hand, to quantify precisely the loading sequence. The experimental setup is pictured in Figure 1.

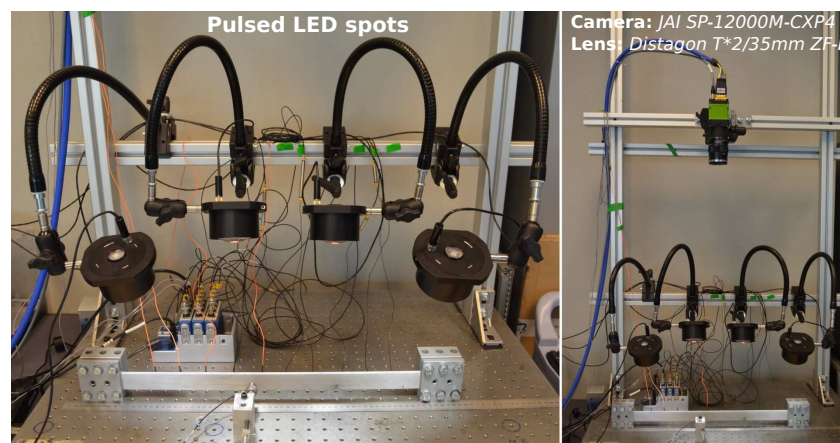


Figure 1. Experimental set-up.

## 2.2. DIC Post-Processing

The DIC method consists in determining a displacement field by comparing a distorted image to a reference one, which can be chosen arbitrarily among all the images of the sequence. In practice, the reference image is recorded before the shock. The images are considered as gray level functions,  $f$  for the reference image and  $g$  for the distorted one, spatially discretized over the pixels of the camera and taking integer values within the dynamic range of the digitisation provided by the camera (here 8 bits). Numerous formulations and implementations of DIC are available, a short review of which can be found in [14]. For the present study, the in-house software CMV has been used. This software has initially been specifically developed for micromechanical applications using scanning electron microscope (SEM) images or images recorded with optical microscopes (see, e.g., [15–17] for applications). It implements several DIC formulations and has been shown to provide results consistent with other implementations (it is one of the software packages bench-marked in [14]). In addition, some specific post-processing routines adapted to micromechanical analyses are implemented, out of the scope of the present work, as well as routines to efficiently quantify the measurement errors, including random and systematic errors [16], which will be discussed later.

The particular DIC formulation used in this study consists in dividing the region of interest of the reference image into juxtaposed independent, and in practice square, correlation windows. The size of these windows needs to be sufficiently large with respect to the local gray level fluctuations of the images and sufficiently small with respect to the fluctuations of the displacement field to be investigated. Within each of these windows, the mechanical transformation  $\Phi_0$  is assumed to be a purely rigid translation (transformation of order 0, see [14]) characterized by two scalar components. The actual mechanical translation of the beam is estimated by maximizing the matching between the reference  $f$  and the back-translated deformed image  $g(\Phi_0)$ , the matching being quantified by the so-called zero-centered, normalized cross-correlation coefficient,  $C$ , defined as:

$$C = 1 - \frac{\int_D (f(\underline{u}) - \bar{f})(g(\Phi_0(\underline{u})) - \bar{g}) du}{\sqrt{\int_D (f(\underline{u}) - \bar{f})^2 du \int_D (g(\Phi_0(\underline{u})) - \bar{g})^2 du}} \quad (1)$$

where  $\bar{f}$  and  $\bar{g}$  are the mean values of  $f(\underline{u})$  and  $g(\Phi_0(\underline{u}))$  in the current window, with  $\underline{u}$  the coordinates vector, and  $\int_D$  refers to a summation over all pixels in the reference window.

We emphasize here the fact that higher-order shape functions describing the mechanical transformation with, e.g., affine or quadratic functions were unnecessary because of the very low strains associated with the vibrations of the beam. The actual DIC errors are for the present application dominated by the so-called “ultimate errors” and not the shape function mismatch errors: we refer to [14] for a discussion on these two error regimes. This has been checked with a comparison of the displacements evaluated assuming a rigid transformation and those obtained when an affine transformation is assumed, whose higher-order coefficients are determined, not by optimizing the correlation coefficient (which would have led to additional random errors, see [14]), but from a larger scale fitting using the displacements evaluated in neighbor windows (see [18] for details about such a procedure). The differences between both approaches are within the random errors, discussed hereafter. This proves that the DIC errors in our experiments are identical to those occurring when purely rigid translations are considered, i.e., DIC errors are governed by the so-called ultimate error regime [14].

It is then of primary importance to consider the parameters that govern the accuracy in this regime: the quality of the speckle pattern, image noise, window size, and gray level interpolation used in the DIC formulation. The latter is central to the evaluation of displacement with subpixel accuracy, as it allows us to compute  $g(\Phi_0(\underline{u}))$  for integer pixel positions  $\underline{u}$  in the reference image, even when  $\Phi_0$  is a subpixel translation. The CMV software provides several options for the interpolation of gray levels, which have been compared. It turns out that an interpolation with bi-quintic splines provides the best results



here. As already discussed, the image noise has been reduced to a minimum for the chosen cameras, using appropriate lighting. The main way to further optimize the experiment is then to consider the speckle painting and the window size.

### 2.3. Speckle Choice and Characterization

The image contrast, provided here by a speckle painting as the non-painted beam does not provide sufficiently pronounced gray level fluctuations, plays a central role in the DIC measurement accuracy. It is usually designed to be random, to avoid mismapping between patterns of similar shapes, even though a periodic pattern could also be considered by the CMV software (e.g., [19]). Periodic patterns are also easier to produce, and several methodologies are compared here. Indeed, as shown in several studies [14,20,21], the spot diameter directly affects the performance of the full-field measurements and the pattern size that can be used. Most of the speckles are made black on white. Crammond et al. [21] show four experimental speckles: two white on black and two black on white. The results show that the spots' size and distribution are more prominent than the colors of the spots and the background. In order to determine the quality of our speckle, three different ones were made on an aluminum piece: one with spray paint, which is the most-used technique [22], another with a black fine felt tip pen, and the last with a sponge. These three examples are visible in Figure 2a–c.

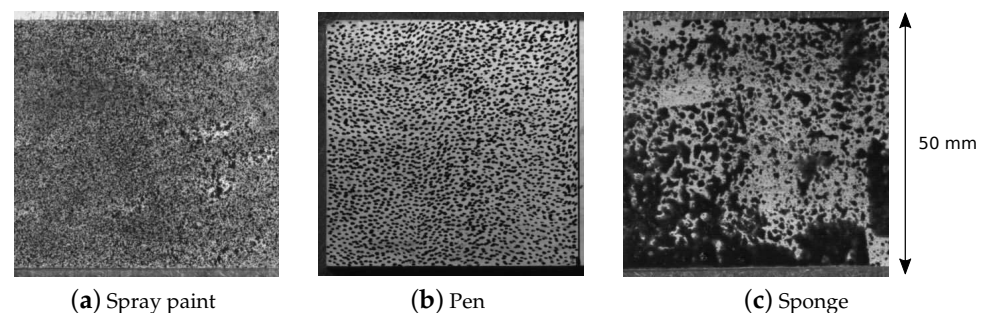


**Figure 2.** Experimental speckles on aluminum piece.

To measure the error and the uncertainty of the measured in-plane displacements the procedure described in [16] is adapted to the present set-up. It consists in applying a slight magnification achieved by moving the camera, mounted on a linear translation stage with micrometer resolution, towards the target object. In this way the object seems to be bigger. Thus, the apparent transformation of the sample is homogeneous and the displacement measured at each point can be compared with the one expected. In this case the camera is translated 6 mm closer to the aluminum piece, so the homogeneous apparent deformation is about 0.5%, and the DIC is performed on a  $350 \text{ px}^2$  square area with 50 patterns in both directions. The distribution of the subpixel displacement is shown on Figure 3 in the pen case. Here, the subpixel displacement is divided into ten parts. Figure 3 clearly indicates that the obtained distribution is quite homogeneous for each part. It is then possible to determine the systematic error (see Figure 4a–c) and the measurement uncertainty (see Figure 4d–f) [23] for the different speckles applied and for different pattern sizes (10, 15, 20, and  $25 \text{ px}^2$ ). The black horizontal line in Figure 4f represents the maximum value of the y-axis of Figure 4d,e. These figures represent, respectively, the means and the standard deviations of the error for each subpixel part.

It can be concluded from Figure 4 that the speckle made using the pen is the most beneficial to our experimental configuration. Indeed, the systematic error is always less than 0.01 px in this case (Figure 4b), whereas it can be up to the order of 0.02 px for the speckles using spray paint and the sponge (Figure 4a,c respectively). The value of the measurement uncertainty is between 0.005 and 0.01 px for the speckle using a pen. As expected, the uncertainty decreases with the increase in the size of the patterns. The uncertainty obtained considering the spray paint speckle (Figure 4d) is slightly higher

and is much more important with the sponge speckle (Figure 4f). As the best results are obtained with the speckle realized with the pen, this technique was therefore chosen to be applied to the tested beam. We have also chosen patterns of 20 px<sup>2</sup> in order to, on the one hand, obtain a low uncertainty and, on the other hand, place several elements in the thickness of the beam. This leads to an accuracy of the DIC slightly lower than one hundredth of a pixel. As the ratio mm/pixel is equal to 0.125 in our images, a displacement measurement accuracy of 1.25 μm is expected. The speckle obtained for the experiments is described by the following characteristics: the density is equal to 1.86 spots/mm<sup>2</sup> or 0.029 spot/px<sup>2</sup>, the size of the spots (diameter) is between 3 and 7 px, and the proportion of the black spots on the white background is about 32%. Concerning the image and especially the white and black contrast, there are approximately 140 gray levels (out of 256) between the mean value of the gray level of the black spots and the mean value of the gray level of the white background.

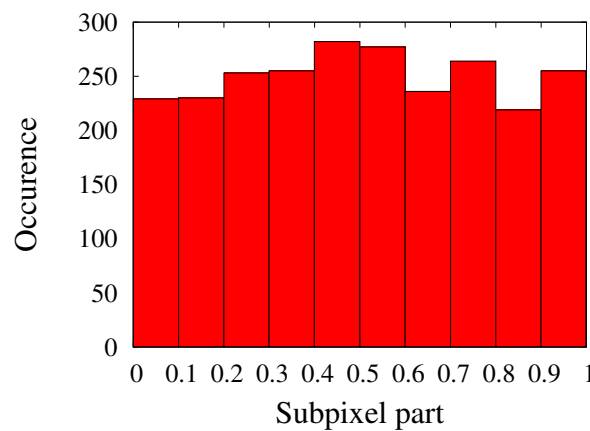


Figure 3. Distribution of subpixel displacement.

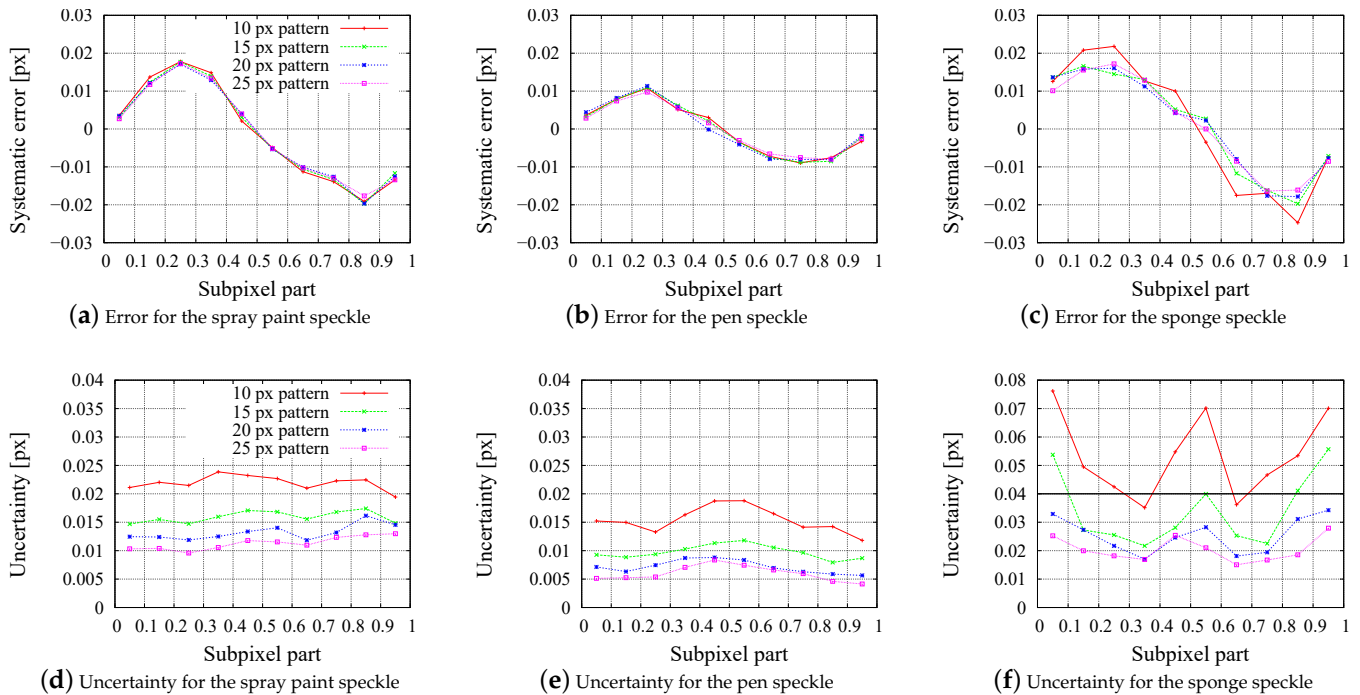
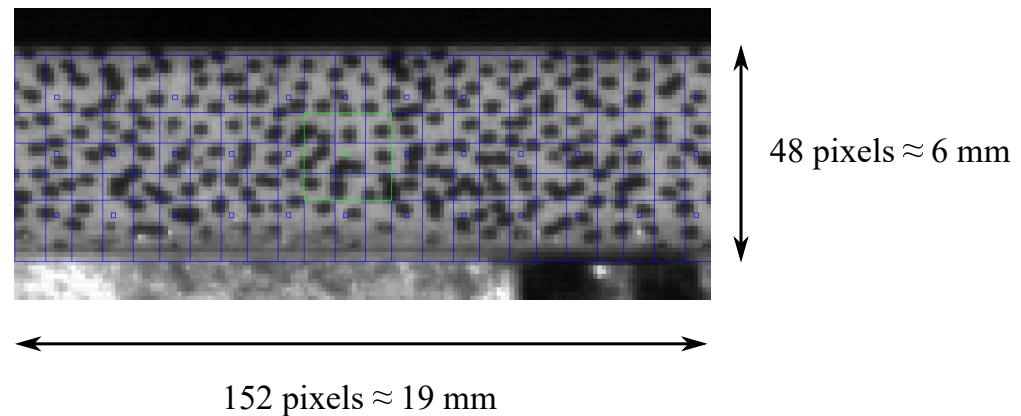


Figure 4. Systematic errors and uncertainties for different experimental speckles and different pattern sizes.

### 2.4. Full-Field Measurements

Concerning the full-field measurements, the area of interest, which represents the beam, is decomposed into 900 patterns: 300 patterns in length over 3 levels in thickness. In this configuration, full-field measurements involve 90 times more points than the instrumentation with accelerometers. However, in this study, we will only consider the results obtained from the 300 points close to the neutral axis; therefore, the configuration only involves 30 times more points. The DIC is performed with patterns of  $20 \text{ px}^2$  in size, using biquintic splines to interpolate the gray levels, and assuming rigid transformations. A zoom of the speckle and the patterns used for the DIC is shown in Figure 5.



**Figure 5.** Zoom on an image captured by the camera.

Before making any use of these fields, the rigid body motion has to be taken into account. Indeed, the hammer impact sets in motion the frame on which the camera is installed. To compensate for this induced motion, the mean displacement of the clamped points is subtracted to the whole displacement field in both directions of the plane filmed by the camera. The deflections obtained at different times for the clamped–clamped beam are depicted in Figure 6.

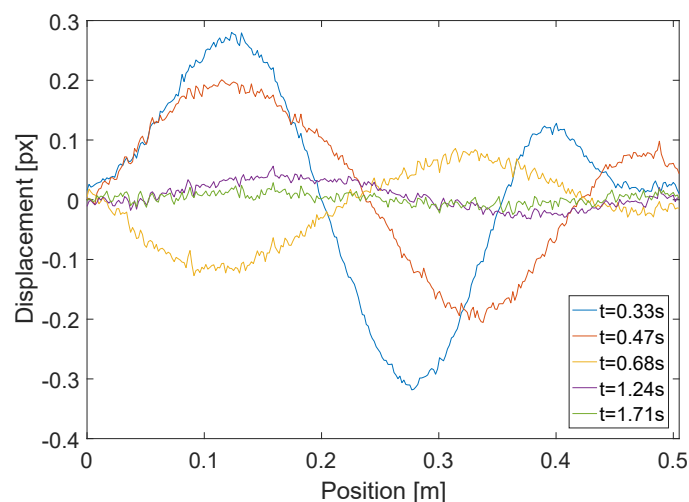


**Figure 6.** Example of deflections obtained for the clamped–clamped beam at different times.

## 3. Modal Identification

### 3.1. Beam Theory

The transverse displacement of a beam due to bending vibration,  $v(x, t)$ , can be decomposed on a modal basis [24] as:

$$v(x, t) = \sum_{i=1}^{\infty} b_i(t) \cdot \phi_i(x) \quad (2)$$



where  $b_i(t)$  is the modal response of the  $i$ th mode and  $\phi_i(x)$  is the  $i$ th mode shape admitting for generic solution:

$$\phi_i(x) = C_1 \cos(\beta_i x) + C_2 \sin(\beta_i x) + C_3 \cosh(\beta_i x) + C_4 \sinh(\beta_i x) \tag{3}$$

The coefficients  $C_i$  depend on the boundary conditions. Applying the boundary conditions for a clamped–clamped beam leads to:

$$\cos(\beta_i L) \times \cosh(\beta_i L) = 1 \tag{4}$$

and for a cantilever beam:

$$\cos(\beta_i L) \times \cosh(\beta_i L) = -1 \tag{5}$$

The values  $\beta_i L$  are the roots of these equations and give the different natural frequencies, with  $L$  the length of the beam. For these two boundary conditions, the  $i$ th mode shape can then be expressed by:

$$\phi_i(x) = \cosh(\beta_i x) - \cos(\beta_i x) - \sigma_i \cdot (\sinh(\beta_i x) - \sin(\beta_i x)) \tag{6}$$

with  $\sigma_i = \frac{\cosh(\beta_i L) - \cos(\beta_i L)}{\sinh(\beta_i L) - \sin(\beta_i L)}$  for a clamped–clamped beam and  $\sigma_i = \frac{\sinh(\beta_i L) - \sin(\beta_i L)}{\cosh(\beta_i L) + \cos(\beta_i L)}$  for a cantilever beam.

The first six natural frequencies expected for the studied beam, in both configurations, are reported in Table 1, as well as the values of  $\beta_i L$  and  $\sigma_i$ . Moreover, the mode shapes are shown on Figure 7 for both configurations.

**Table 1.** Expected natural frequencies.

$i$	Clamped–Clamped Beam			Cantilever Beam		
	$\beta_i L$	$\sigma_i$	$f_i$ [Hz]	$\beta_i L$	$\sigma_i$	$f_i$ [Hz]
1	4.730	0.9825	124.6	1.875	0.7341	15.37
2	7.853	1.0008	343.4	4.694	1.0185	96.3
3	10.996	1.0000	673.3	7.855	0.9992	269.7
4	14.137	1.0000	1112.9	10.996	1.0000	528.6
5	17.279	1.0000	1662.6	14.138	1.0000	873.7
6	20.421	1.0000	2322.1	17.280	1.0000	1305.1

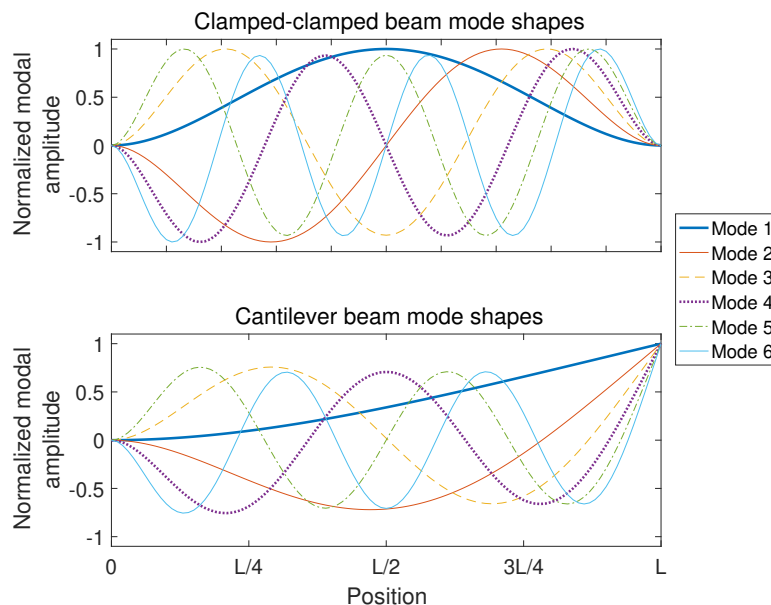


**Figure 7.** Theoretical mode shapes for clamped–clamped and cantilever beams.

### 3.2. Continuous Wavelet Transform Method for Modal Identification

In order to obtain the experimental modal parameters of the beam, a modal analysis is carried out using a method based on the continuous wavelet transform (CWT) [25]. It consists in transforming a signal  $u(t)$  using functions, which are expressed as:

$$\psi_{(b,a)} = \frac{1}{a} \psi\left(\frac{t-b}{a}\right) \tag{7}$$

where  $a$  is a dilating scale parameter,  $b$  is a translation parameter (in time), and  $\psi$  is the mother wavelet.

The mother wavelet must be a square-integrable and piecewise continuous function. For modal identification purposes using the free responses of a system with several degrees of freedom, the mother wavelet has to satisfy certain conditions, which are discussed in [25]. The Cauchy mother wavelet, defined by  $\psi(t) = (i/(t+i))^{n+1}$  with  $i$  the unit imaginary number, is then used in this study.

The CWT can be expressed as:

$$T_\psi[u](a,b) = \frac{1}{a} \int_{-\infty}^{+\infty} u(t) \bar{\psi}\left(\frac{t-b}{a}\right) dt \tag{8}$$

where  $\bar{\psi}(\cdot)$  is the complex conjugate of the function  $\psi(\cdot)$ .

The local resolution of the CWT, in time and in frequency, depends on the dilatation parameter  $a$  and is determined, respectively, by the duration  $\Delta t_\psi$  and bandwidth  $\Delta\omega_\psi$  of the mother wavelet:

$$\Delta t = a\Delta t_\psi \quad ; \quad \Delta\omega = \frac{\Delta\omega_\psi}{a} \tag{9}$$

The factor  $Q$  is introduced as the ratio of the center-frequency to the frequency bandwidth

$$Q = \frac{\omega_\psi}{2\Delta\omega_\psi} = \frac{n + \frac{1}{2}}{\sqrt{2n + 1}} \text{ for Cauchy mother wavelet} \tag{10}$$

In order to avoid edge effects,  $Q$  needs to fulfill certain basic preconditions, which are:

$$c_f \frac{\omega_i}{2d\omega_i} \leq Q \leq \frac{T_f \omega_i}{2c_t} \tag{11}$$

where  $c_t$  and  $c_f$  are two chosen coefficients, here both equal to 5 (see [25]),  $T_f$  is the length of the signal, and  $d\omega_i = \min(\omega_{i+1} - \omega_i, \omega_i - \omega_{i-1})$ .

For each mode, a local CWT is performed in a specific range of time and frequency by adjusting the length of the signal processed, the frequency bandwidth, and the factor  $Q$ . Then, it is possible to extract the modal parameters from each measurement point to obtain the eigen frequencies, the modal damping ratios, and the mode shapes. In the case of free response at point  $j$  of the beam, of abscissa  $x_j$ , Equation (2) leads to:

$$\begin{aligned} v(x_j, t) = v_j(t) &= \sum_{i=1}^{\infty} v_{ji}(t) = \sum_{i=1}^{\infty} \rho_i \exp(-\xi_i \omega_i t) \cos(\tilde{\omega}_i t - \varphi_i(t)) \cdot \phi_i(x_j) \\ &= \sum_{i=1}^{\infty} A_{v_{ji}}(t) \cos(\alpha_{ji}(t)) \end{aligned} \tag{12}$$

where  $\omega_i$  and  $\tilde{\omega}_i$  are the undamped and damped vibration angular frequencies of the  $i$ th mode,  $\xi_i$  is the damping ratio,  $\rho_i$  is a factor depending on initial conditions, and

$$\begin{cases} A_{v_{ji}}(t) &= |\phi_i(x_j)| \rho_i \exp(-\xi_i \omega_i t) \\ \alpha_{ji}(t) &= \tilde{\omega}_i t - \varphi_i(t) + \frac{\pi}{2} (1 - \text{sign}(\phi_i(x_j))) \end{cases} \tag{13}$$

With the assumption of low damping ( $\xi_i \ll 1$ ), each component  $v_{ji}(t)$  can be considered as asymptotic; thus,  $Z_{ji}(t) \approx A_{v_{ji}}(t) \exp(\alpha_{ji}(t))$  where  $Z_{ji}(t)$  is the analytical signal of  $v_{ji}(t)$ .

Then, the modal parameters can be identified using the CWT method. The instantaneous frequency is obtained using:

$$\tilde{\omega}_j = \dot{\alpha}_{ji}(t) = \frac{K}{a_{rv_{ji}}(t)} \tag{14}$$

with  $K$  a constant depending on the mother wavelet and  $a_{rv_{ji}}(t)$  the time evolution of the ridge. For  $\dot{\alpha}_{ji}(t)$ , the dot represents the derivative with respect to time. The skeleton of the wavelet transform is the restriction of the CWT to each ridge and contains a maximum of information, very close to the signal components.

The amplitude along the ridge is used to obtain the modal damping ratio and the mode shape amplitude using the expressions:

$$\log(A_{v_{ji}}(t)) = \log(|\phi_i(x_j)|\rho_i) - \zeta_i\omega_i t \tag{15}$$

$$|\phi_i(x_j)| = \frac{A_{v_{ij}}(t)}{A_{v_{mj}}(t)} \tag{16}$$

where  $A_{v_{mj}}(t)$  is the maximum modal amplitude among the measurement points analyzed.

The instantaneous frequency and the amplitude  $A_{u_{ij}}(t)$  (in log scale) are depicted in Figure 8 for 300 measurement points of the neutral axis of a clamped–clamped beam, for Modes 2 and 5, respectively.

Since the method is a time–frequency method, the results obtained for the eigen frequencies, modal damping ratios, and modal amplitudes depend on time. Thus, to obtain the value of the modal parameters for a measurement point, an average is taken over a time period not subjected to edge effects of the CWT (depending on factor  $Q$  and inside the red vertical lines of Figure 8a–d). For more details on the method, one can see [25].

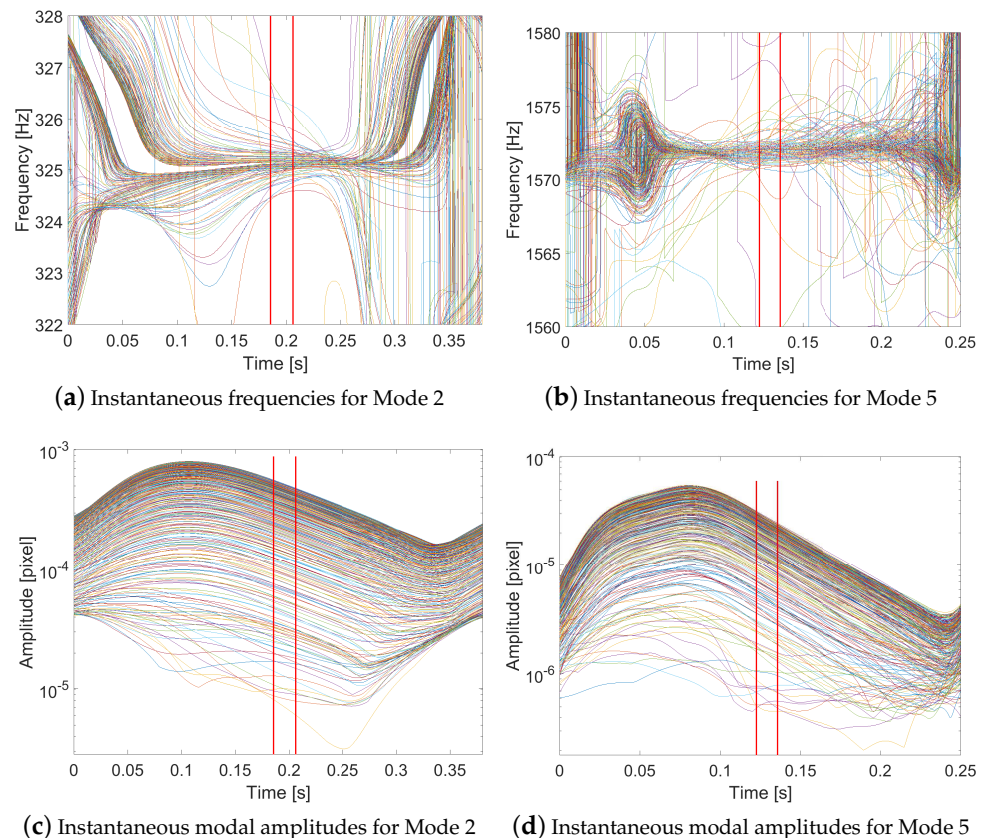


**Figure 8.** Instantaneous frequencies and modal amplitudes (in log scale) obtained from 300 measurement points of the neutral axis of a clamped–clamped beam for Mode 2 and 5.

### 3.3. Signal Processing Procedure to Limit the Disturbance of Measurement Noise on Modal Identification

In order to process the numerous measurement points resulting from DIC, a signal processing procedure is proposed. Indeed, the number of points being much more numerous (several hundreds) than classically with accelerometers (at best several tens of points), some of them are located near the nodes of the different mode shapes and, thus, disturb a global procedure as they contain low information due to a poor signal-to-noise ratio (SNR) due to their location, especially for the higher modes.

The process using the CWT method proposed here, for each mode, is as follows:

- First of all, the length of the signals to be processed has to be fixed, i.e., the beginning and the end of the signals have to be defined. There is no particular difficulty for the beginning of the signal. For the end of the signal, a first wavelet transform is applied to all the measurement points on a narrow frequency bandwidth close to the frequency of the mode considered ( $[0.99, 1.01] \times f_i$ ) with a factor  $Q = (Q_{min} + Q_{max})/5$ . Then, after a first approximation of the mode shape, the points whose modal amplitude is less than 0.1 (the mode shape is normalized to the maximum value, so its maximum is equal to 1) are not used for determining the end of the signals. For each of the remaining points, the curve  $\log(A_{u_{kj}}(t))$  is normalized to the maximum and the time from which the curve is under the arbitrarily fixed threshold of 0.2 is saved. The final time for all the points to be analyzed is defined as the minimum of the times saved previously.
- Once the length of the signals is determined, a second wavelet analysis on the same bandwidth as before is performed using a factor  $Q$  equal to  $0.95 \times Q_{max}$  in order to minimize the time fluctuation on the ridge. The values obtained for the modal parameters (frequency, modal damping ratio, and mode shape) are the averages of these parameters for the time interval not subject to edge effects (inside the two vertical red lines represented in Figure 8).
- In order to limit the noise disturbance on the identification of the modal parameters, a singular value decomposition (SVD) is applied to the wavelet scalogram as proposed in [26]. The scalogram is recombined from matrices obtained using SVD after setting the lowest singular values to zero. Since it is time-consuming and not needed for the first wavelet transform used to determine the final duration of the signals, the SVD is only applied for the second wavelet transform used to obtain the modal parameters. The noise present in the data has no effect on the determination of the frequency, a small effect on the mode shape (Figure 9a,b (zoom)), and a quite important effect on the values of the modal damping ratio (Figure 9c).

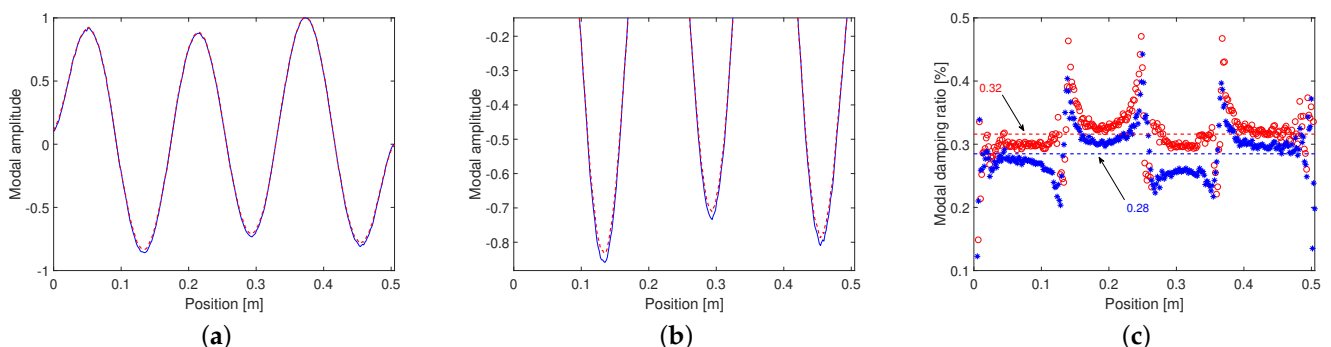


**Figure 9.** Comparison of the results obtained for the clamped–clamped beam with (red dash curves or circles) and without (blue curves or asterisks) the use of SVD for denoising: (a,b) mode shape of Mode 6 and (c) modal damping ratio of Mode 4.

Another point to pay attention to is the analysis of the results in terms of statistics, in particular the dispersion of the results due to the large number of measurement points. Indeed, as the mode shapes obtained are quite noisy, if they are normalized to the maximum without precaution, a higher relative standard deviation (RSD) would result (Figure 10a).

To avoid this, the mode shapes are filtered with a low-pass filter to remove the noise disturbance and the normalization factors are deduced from these filtered mode shapes. The low-pass filter is applied by performing zero-phase digital filtering by processing the input data, i.e., the mode shapes, in both the forward and reverse directions (filtfilt function in MATLAB®). The filter used in the filtfilt function is a 4th-order lowpass elliptic filter (ellip function in MATLAB®) with 0.5 dB of passband ripple, 40 dB of stopband attenuation, and a passband edge spatial frequency of 20 m<sup>-1</sup>, which, for mode shapes sampled at nearly 592 m<sup>-1</sup>, corresponds to 0.068π rad/sample. Figure 10b shows the mode shape of Mode 6 of the clamped–clamped beam for ten tests after applying this normalization. Finally, the relative standard deviation is calculated. Figure 11 illustrates, in log scale along the y-axis, the relative standard deviation obtained for ten tests before and after the renormalization of four mode shapes of the clamped–clamped beam.

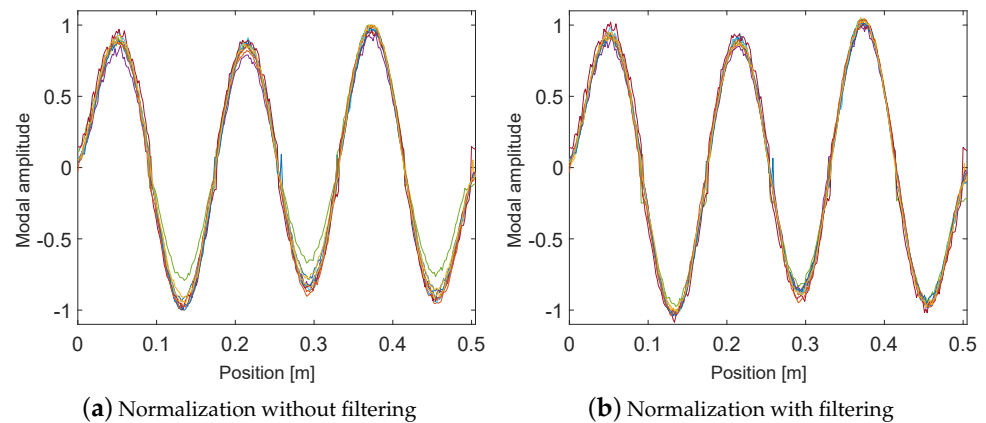


**Figure 10.** Comparison of different normalization criteria on the dispersion obtained for ten tests for mode shape of Mode 6 of the clamped–clamped beam.

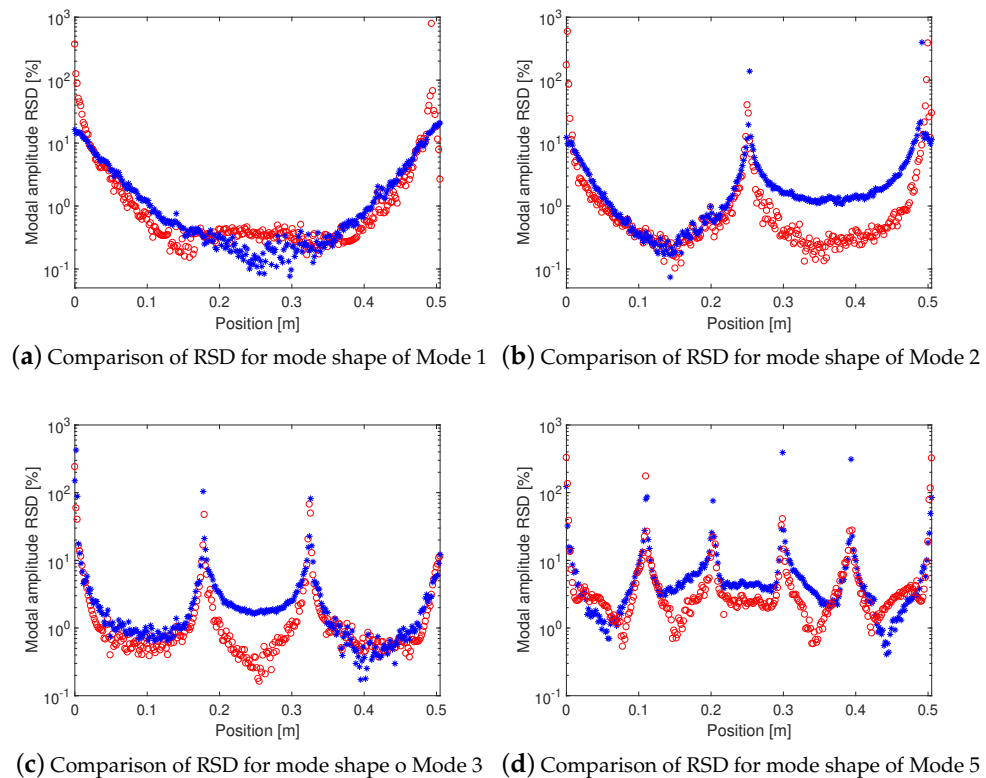


**Figure 11.** Comparison of relative standard deviation before (blue asterisks) and after (red circles) the renormalization of mode shapes obtained for ten tests.



The number of measurement points to take into account in the calculation of the average and the relative standard deviation of modal damping ratio is also important. The frequency being a more stable modal parameter, the average frequencies are not sensitive to the number of points used to calculate them. Figure 12 shows the evolution of the average modal damping ratio for the first six modes of the clamped–clamped beam according to the number of measurement points taken into account in the calculation. As the information is better when the modal amplitude is greater, the measurement points used for the calculation of frequencies and modal damping ratios are selected based on their modal amplitude using a threshold (equal to 0.5).

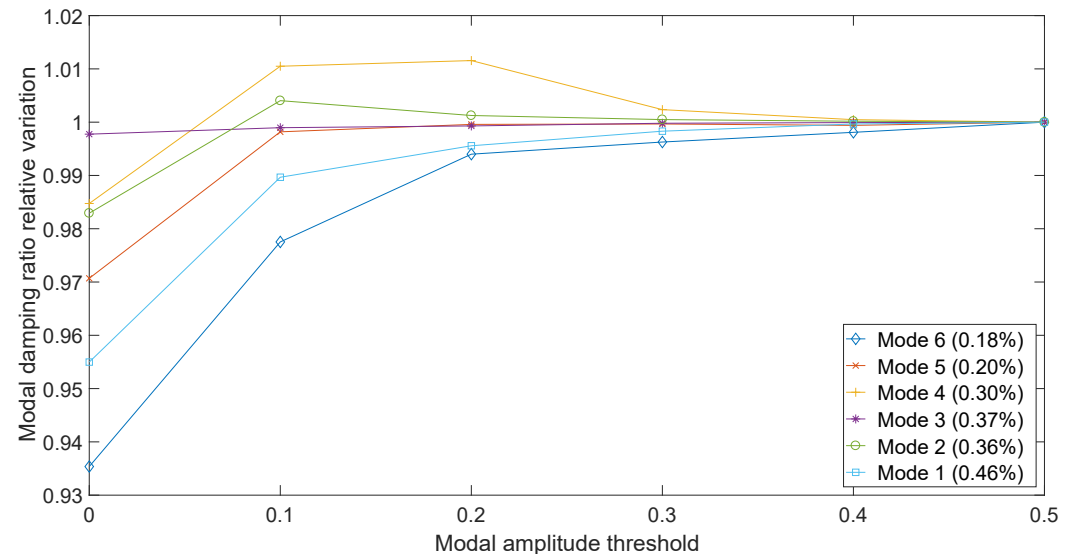


**Figure 12.** Relative variation of the modal damping ratios of the clamped–clamped beam as a function of the modal amplitude threshold of the normalized mode shapes used to select the points to calculate the averages of the modal damping ratios.

This analysis is performed on the two data sets obtained from full-field measurements and accelerometers.

#### 4. Results and Discussion

Two cases are studied, i.e., a clamped–clamped beam and a cantilever beam, with ten tests being performed for each case. The mean and the standard deviation for each modal parameter are determined in order to evaluate the tests' repeatability.

##### 4.1. Clamped–Clamped Beam

First, a 1D FE computation, using beam elements with two degrees of freedom, is performed and compared with the results of the test. The loading signal is taken up from the experimental measurement of the impact hammer. To fit the numerical model on the experimental configuration, the Young's modulus is adjusted in order to obtain the first numerical frequency in accordance with the experimental one. On Figure 13 the Fourier transform of both numerical and experimental data, for the neutral axis point of coordinate  $x = 14.10$  cm, are shown. The first six modes are observable through the experimental displacement field. Figure 14 illustrates the comparison between numerical and experimental transverse displacements of the middle of the beam ( $x = L/2 = 25.25$  cm). Concerning the experimental displacements, the standard deviation before the excitation, representing the noise level, is lower than  $10^{-6}$  m, as expected. The results presented in the two previously mentioned figures show a very good agreement of the measurement with the theory, except for Mode 4, whose amplitude is higher in the experiment, possibly due to a spurious mode.

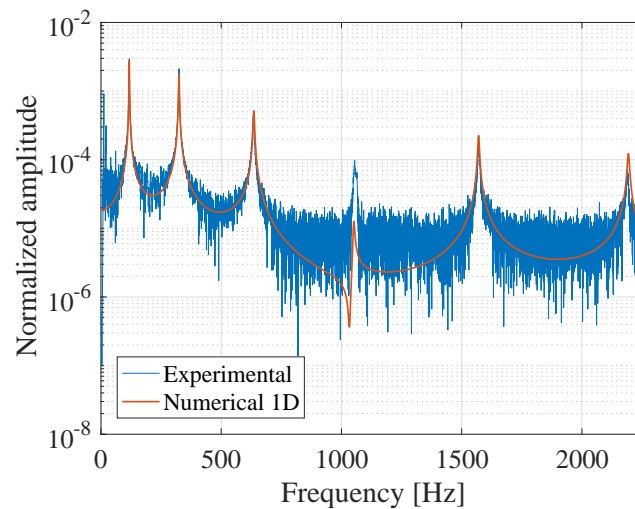


**Figure 13.** Comparison of Fourier transform of numerical and experimental signals for neutral axis point of the clamped–clamped beam at abscissa  $x = 14.10$  cm.

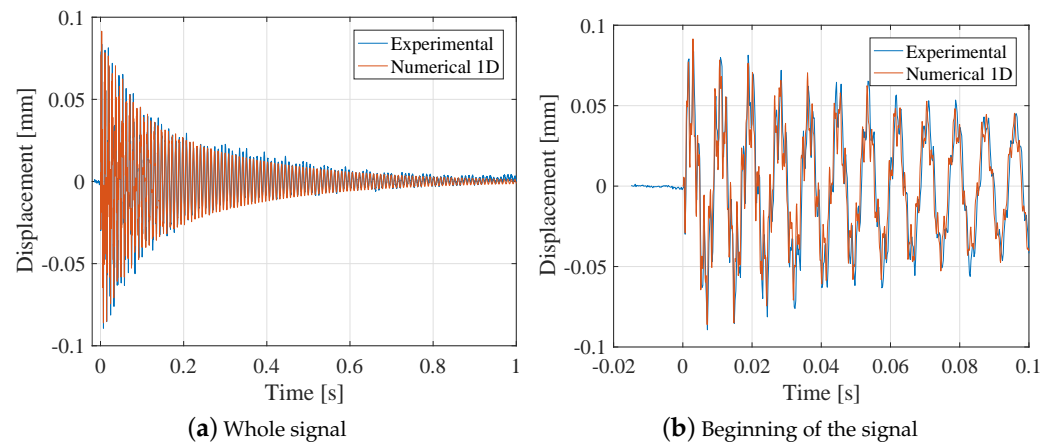


**Figure 14.** Comparison of numerical and experimental transverse displacement for the neutral axis point of the clamped–clamped beam at abscissa  $x = 25.25$  cm.

In order to quantify the noise level for each mode for the full-field measurements, the SNR is calculated for each measurement point of the neutral axis for the clamped–clamped beam. The evolution of this ratio along the beam is shown for each mode on Figure 15a for the full-field displacements and Figure 15b for the accelerometers for comparison. For the full-field displacements, it can be observed that this ratio decreases with the mode number and also at the modal nodes. These two observations can be easily explained by the fact that the higher the mode is, the less it participates in the global motion and that, close to the nodes, the motion is near to zero and thus, closer to the noise level.

After evaluating the noise level for each mode, the modal parameter identification is presented. Figure 16a,d depict, for a specific test, the frequency determined at each measurement point for the second and fifth mode, respectively. Figure 16b,e show the damping ratios and Figures 16c,f the mode shapes for the same modes, respectively. From these figures, it can be observed that, apart in a few measurement points near the modal nodes and the boundary conditions, the determined frequencies and damping ratios are rather constant. In the following, the frequencies and modal damping ratios will refer to the averages of the values obtained for all measurement points.

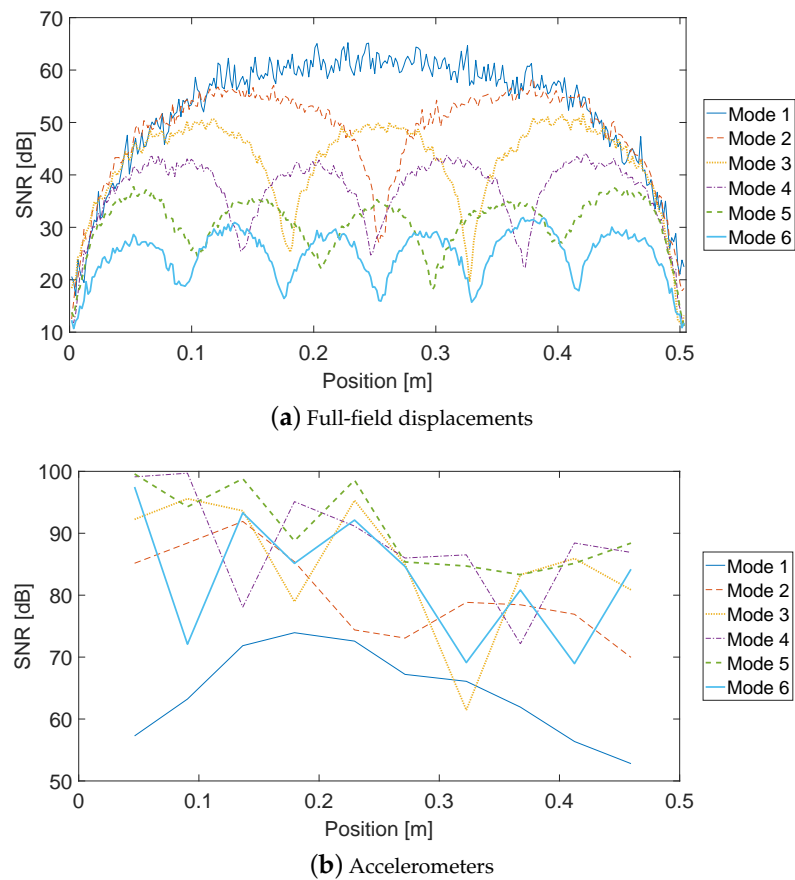


**Figure 15.** Signal-to-noise ratio (SNR), in dB, for different measurement types for the clamped-clamped beam: (a) full-field displacements and (b) accelerometers.

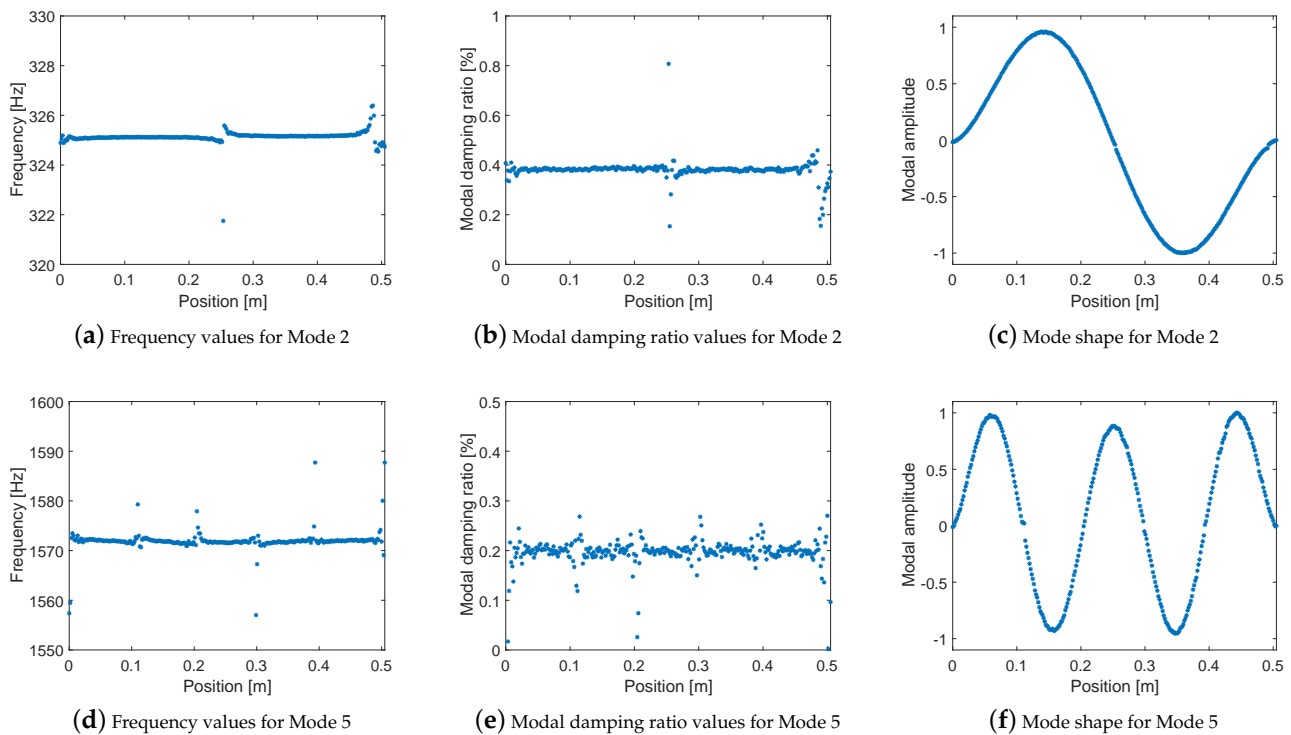


**Figure 16.** Modal parameters obtained from the DIC measurements for Modes 2 and 5 of the clamped-clamped beam.

The distributions of the frequency and the damping ratio values obtained for the second and fifth mode are shown in Figure 17a,d. It appears one more time that, apart from a few points very far from the average values, there is little deviation for all other points.

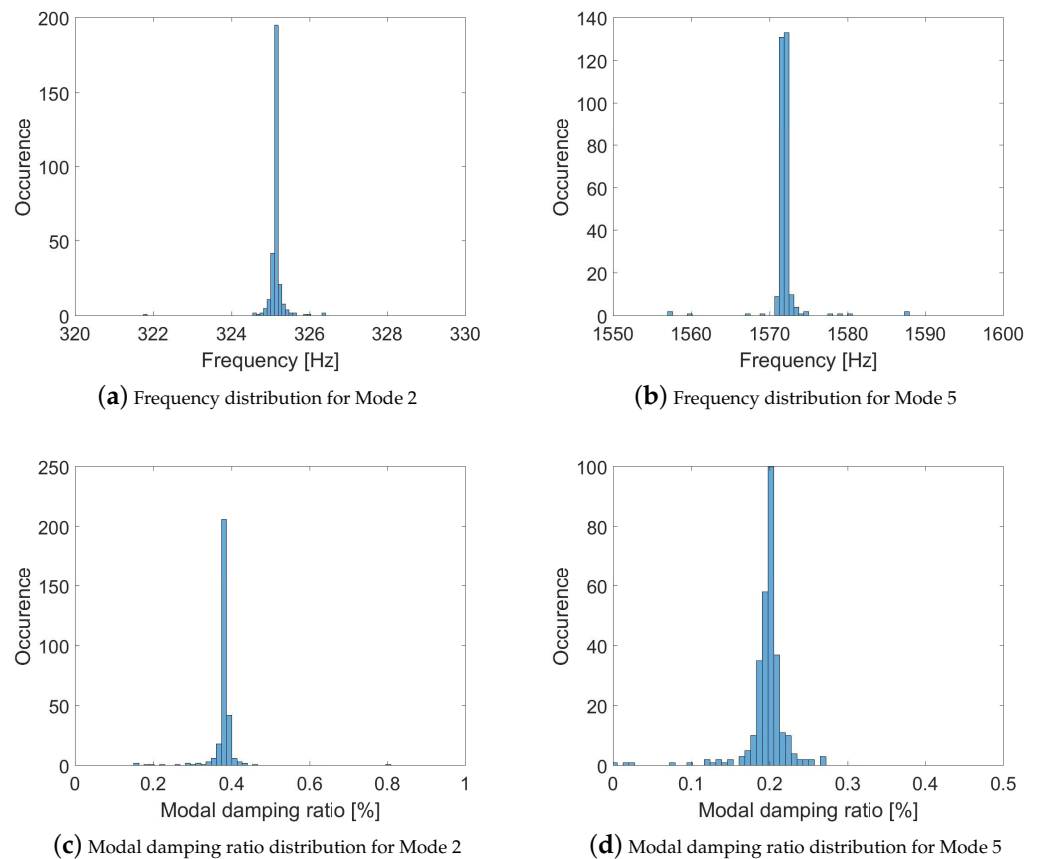


**Figure 17.** Distributions of frequencies and modal damping ratios obtained from the DIC measurements for Mode 2 and 5 of the clamped–clamped beam.

One of the main advantages of a full-field measurement is to consider numerous points and thus to provide mode shapes with a high discretization. Figure 18a,f show the means and relative standard deviations (RSD) for each point of the mode shapes over ten tests. Since the CWT method is an output-only method, which means that the excitation signal is not needed for modal parameter identification, the mode shapes are normalized to their maximum ( $L_1$ -normalization). The mode shapes obtained are consistent with those expected. Considering the standard deviation, the figures highlight that, as expected, it increases with the order of the mode, because the SNR is less important for higher modes, and also close to the modal nodes.

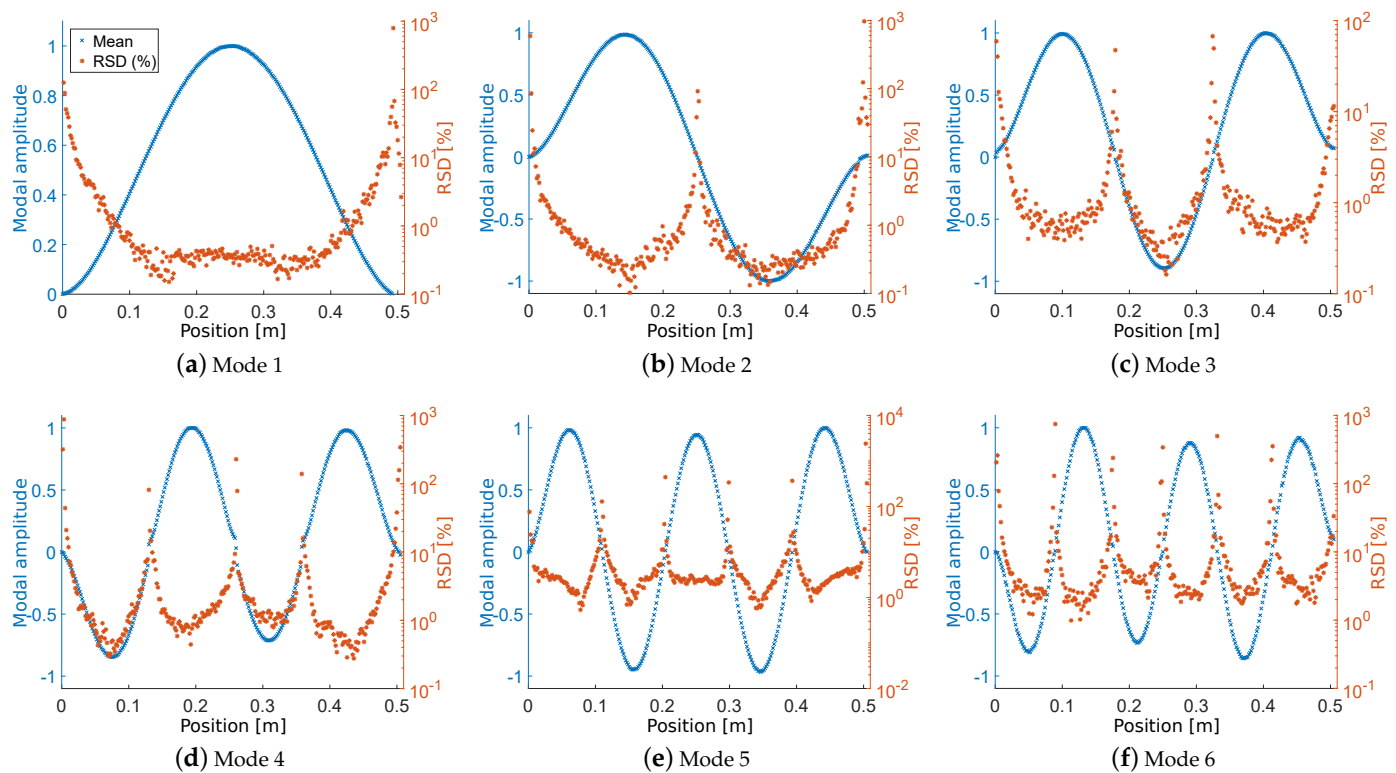


**Figure 18.** First six mode shapes obtained from the DIC measurements for the clamped–clamped beam.

For the frequencies and damping ratios, the values obtained from the DIC measurements and the accelerometers are reported in Tables 2 and 3, respectively.

**Table 2.** Average frequencies (in Hz) determined from DIC measurements and accelerometers for the clamped–clamped beam.

Test	Mode 1		Mode 2		Mode 3		Mode 4		Mode 5		Mode 6	
	DIC	Acc.	DIC	Acc.	DIC	Acc.	DIC	Acc.	DIC	Acc.	DIC	Acc.
1	118.0	118.0	325.1	325.1	634.5	634.7	1055.0	1055.2	1571.8	1572.2	2192.3	2193.4
2	117.9	117.9	324.9	325.0	634.1	634.4	1054.5	1054.8	1571.6	1571.6	2191.3	2192.1
3	117.8	117.8	324.8	324.8	634.0	634.3	1054.7	1054.6	1571.4	1571.6	2191.6	2192.1
4	117.9	118.0	325.0	325.1	634.8	634.8	1055.8	1055.7	1572.8	1572.6	2193.6	2194.3
5	117.8	117.8	324.7	324.7	634.2	634.5	1054.9	1054.9	1572.0	1571.9	2192.4	2193.2
6	117.5	117.6	324.5	324.5	633.8	633.9	1054.2	1054.5	1571.3	1571.1	2191.2	2191.5
7	117.8	117.8	324.8	324.9	634.2	634.3	1054.8	1055.0	1571.6	1571.8	2191.9	2192.5
8	117.6	117.7	324.6	324.7	634.0	634.1	1054.3	1054.5	1571.2	1571.4	2191.0	2192.1
9	117.6	117.6	324.4	324.5	633.6	633.9	1054.1	1054.3	1570.9	1571.2	2189.9	2191.8
10	117.5	117.5	324.3	324.3	633.6	633.7	1054.3	1054.3	1571.0	1571.3	2190.8	2191.9
Mean	117.8	117.8	324.7	324.8	634.1	634.2	1054.7	1054.8	1571.5	1571.7	2191.6	2192.5
RSD (%)	0.15	0.15	0.08	0.08	0.06	0.06	0.05	0.04	0.04	0.03	0.05	0.04

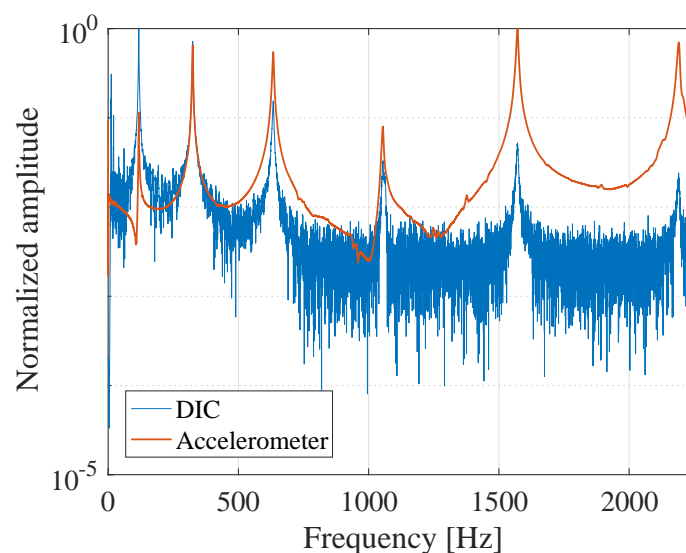


**Table 3.** Average modal damping ratios (in %) determined from DIC measurements and accelerometers for the clamped–clamped beam.

Test	Mode 1		Mode 2		Mode 3		Mode 4		Mode 5		Mode 6	
	DIC	Acc.	DIC	Acc.	DIC	Acc.	DIC	Acc.	DIC	Acc.	DIC	Acc.
1	0.49	0.51	0.38	0.37	0.38	0.37	0.32	0.31	0.20	0.20	0.17	0.18
2	0.51	0.50	0.36	0.36	0.39	0.39	0.32	0.31	0.21	0.21	0.18	0.19
3	0.44	0.46	0.37	0.36	0.39	0.38	0.32	0.31	0.21	0.21	0.18	0.19
4	0.37	0.36	0.26	0.26	0.30	0.33	0.25	0.27	0.18	0.17	0.17	0.17
5	0.37	0.38	0.36	0.36	0.36	0.36	0.30	0.29	0.20	0.19	0.17	0.18
6	0.47	0.48	0.37	0.37	0.39	0.39	0.31	0.30	0.21	0.21	0.18	0.19
7	0.46	0.47	0.37	0.37	0.37	0.38	0.30	0.30	0.20	0.20	0.18	0.19
8	0.51	0.53	0.37	0.37	0.39	0.38	0.31	0.30	0.21	0.20	0.18	0.19
9	0.50	0.55	0.37	0.36	0.38	0.39	0.30	0.30	0.20	0.20	0.17	0.19
10	0.52	0.54	0.37	0.36	0.38	0.38	0.30	0.30	0.20	0.20	0.18	0.19
Mean	0.46	0.48	0.36	0.35	0.37	0.37	0.30	0.30	0.20	0.20	0.18	0.19
RSD (%)	12.20	13.47	10.13	9.59	7.54	4.94	6.95	4.06	4.65	5.46	2.91	4.17

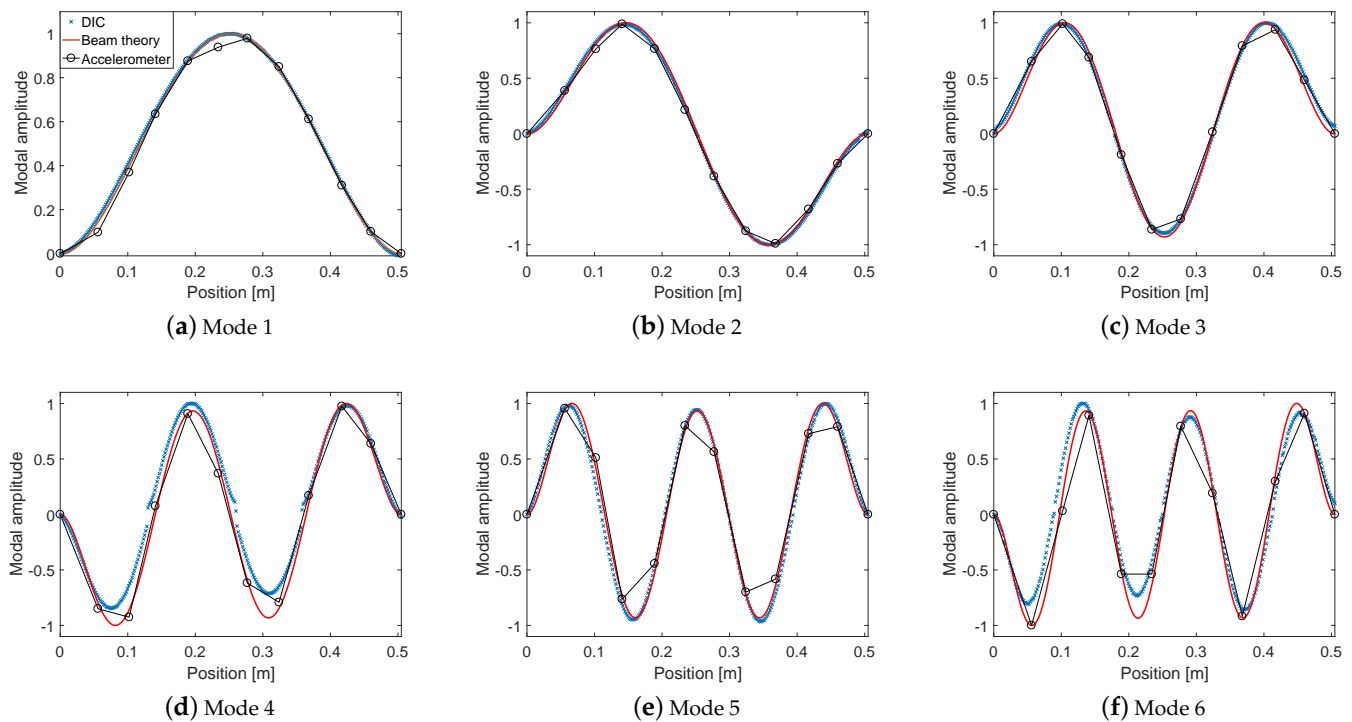
From results reported in the aforementioned tables, a good repeatability of the tests is observed; indeed, the standard deviations of frequencies and of modal damping ratios are low for both data sets. Secondly, it can be seen that the two kinds of measurement lead to very similar results for the natural frequencies and modal damping ratios.

Figure 19 depicts the Fourier transforms of the measured displacement and acceleration for the neutral axis point of the clamped–clamped beam at abscissa  $x = 14.10$  cm. The presented results clearly show that the displacement measurement emphasizes the low frequencies, while the acceleration measurement emphasizes the high frequencies, which is classical. It should also be noted that the SNR is much higher for the acceleration measurement, especially as the mode order increases.

**Figure 19.** Fourier transforms obtained from the accelerometer and the DIC for the neutral axis point of the clamped–clamped beam at abscissa  $x = 14.10$  cm.

To continue the direct comparison between modal analysis based on accelerometers and full-field measurements, Figure 20 presents the first six mode shapes determined from both experimental data sets, for a single test, and those expected from the beam theory. Therefore, the graphs confirm a very good agreement between the experimental measurements and the theory, excepted for the fourth and sixth mode shapes obtained with DIC measurements. Indeed, the excitation level for the sixth mode is very weak so

that the identified mode shape is very noisy and, for the fourth mode, the identification process is disturbed, especially near the modal nodes, by a spurious mode with nearly the same frequency. This spurious mode is only present in the DIC measurements. Its shape is that of a first mode but its frequency does not correspond to the first mode of the other motion components, i.e., traction and torsion. However, we found it was sensitive to the boundary conditions but not enough to uncouple this mode from the fourth mode and improve the identification process.



**Figure 20.** Comparison of the first six mode shapes of the clamped–clamped beam for a particular test.

To validate the use of the DIC to perform modal analysis, we can compare the eigen frequency and modal damping ratio values obtained to those determined using the accelerometer measurements. The mode shapes can also be compared to theoretical or numerical ones. To this end, the Modal Assurance Criterion (MAC) is commonly used [27]. This criterion is defined as the normalized scalar products of the mode shapes. The  $i$ th mode of a family  $A$  is compared to the  $j$ th mode of a family  $B$ , and the resulting scalar is arranged into the MAC matrix as follows:

$$\text{MAC}(i,j) = \frac{|\{\phi_A\}_i^T \{\phi_B\}_j|^2}{(\{\phi_A\}_i^T \{\phi_A\}_i) (\{\phi_B\}_j^T \{\phi_B\}_j)} \quad (17)$$

The values of the MAC coefficients are bounded between 0 and 1, with 1 indicating fully consistent mode shapes. It can only indicate consistency and does not indicate validity or orthogonality. A value near 0 indicates that the modes are not consistent.

Moreover, the MAC can be calculated between both data sets in order to compare the different mode shapes obtained. First, an auto-MAC issued from the DIC mode shapes is shown on Figure 21a. The fact that the values of the non-diagonal terms  $\text{MAC}(1,4)$  and  $\text{MAC}(4,1)$  are a little bit higher, but still very low (around 0.03), than for the other non-diagonal terms is due to the spurious mode perturbing the identification of the fourth mode, as previously discussed. It appears, for the zones near the nodes, that the determination of the fourth mode shapes is disturbed by another mode, whose frequency is close to the fourth mode and whose shape is similar to that of a first mode.

The MAC matrix between the accelerometer and DIC data is presented in Figure 21b. One more time, this latter figure shows a good agreement between both experimental mode shape bases. As for the auto-MAC of DIC, the term  $MAC(1,4)$  is different (also around 0.03) due to the spurious mode observed in DIC measurements. Due to this spurious mode for the fourth mode and to the low quality of the determination of the mode shape for the sixth mode, for DIC measurements, the correlation coefficients for these modes (diagonal terms) are lower than for the other modes (0.99), respectively equal to 0.96 and to 0.94.

The results obtained for this configuration are encouraging, with the first six modes quite well identified, except the sixth one. The natural frequency of the last mode is around 2192 Hz. Following the previous study carried out for clamped–clamped boundary conditions, the next section will focus on the case of the cantilever beam.

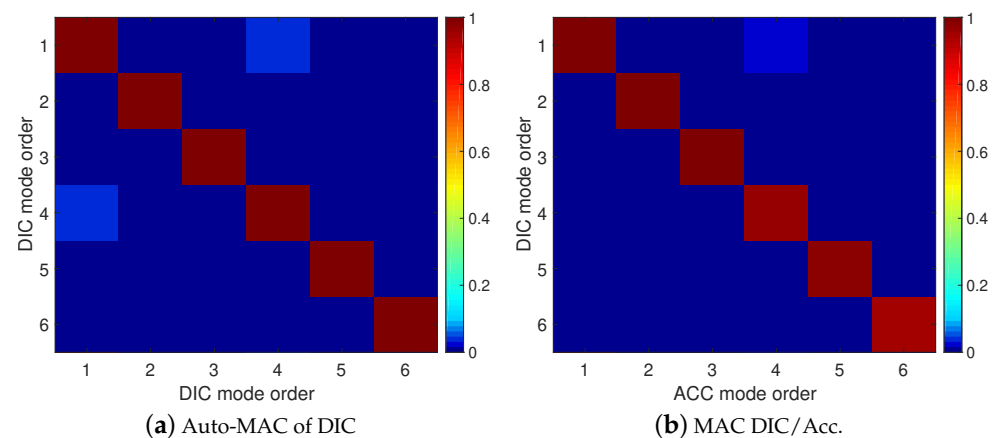


**Figure 21.** Components of the MAC matrix calculated from measurements: (a) auto-MAC of mode shapes obtained from DIC measurements and (b) MAC of mode shapes obtained from accelerometer and DIC measurements.

#### 4.2. Cantilever Beam

Figure 22 shows the averages and standard deviations over the ten tests for the mode shapes, while Tables 4 and 5, respectively, report the frequencies and the modal damping ratios determined using the full-field measurement and the accelerometer data set.

DIC measurements are obtained after a numerical processing performed on each image. The time signal being obtained after a numerical post-processing and not in an analogue way, as for accelerometers, the signal is therefore necessarily subjected to aliasing because no analogue filter can be applied. Thus, the eighth mode observed from DIC measurements, at the frequency of 2178 Hz (see Table 4), is a folding frequency of the frequency obtained with the accelerometer measurements for this mode, which is equal to 2327 Hz.

As for the previous case of the clamped–clamped beam, the tests for the cantilever beam show a good repeatability and both sets of data lead to similar eigen frequencies and modal damping ratios. As in the previous case, the mode shapes were determined with a good accuracy for modes with frequencies up to almost the Nyquist frequency, equal to 2250 Hz in this study.

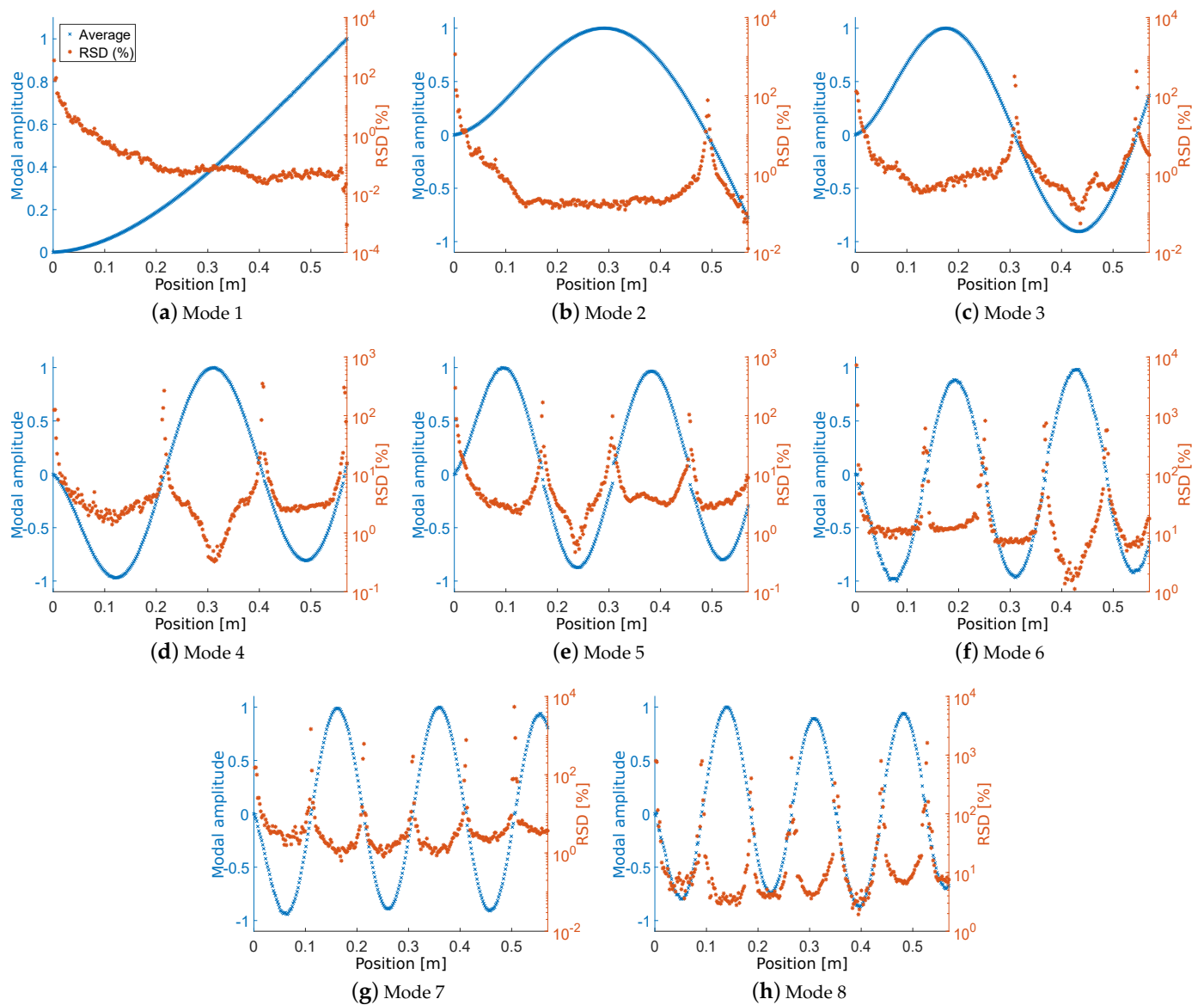


Figure 22. First eight mode shapes obtained from the DIC measurements for the cantilever beam.

Table 4. Frequencies of the cantilever beam determined for the different tests from DIC measurements and accelerometers (in Hz).

Test	Mode 1		Mode 2		Mode 3		Mode 4		Mode 5		Mode 6		Mode 7		Mode 8	
	DIC	Acc.	DIC	Acc.	DIC	Acc.	DIC	Acc.	DIC	Acc.	DIC	Acc.	DIC	Acc.	DIC	Acc.
1	15.05	15.05	93.09	93.08	259.0	259.0	509.3	509.3	844.3	844.3	1255.3	1255.2	1752.9	1753.5	2178.2	2327.0
2	15.04	15.05	93.09	93.08	259.1	259.1	509.4	509.4	844.4	844.2	1255.2	1255.2	1753.2	1753.5	2178.2	2326.9
3	15.04	15.05	93.08	93.10	259.1	259.1	509.3	509.3	844.5	844.2	1255.5	1255.3	1753.0	1753.3	2178.0	2326.9
4	15.04	15.05	93.09	93.09	259.0	259.1	509.2	509.3	844.0	844.3	1254.8	1255.3	1753.0	1753.1	2177.9	2326.4
5	15.05	15.05	93.09	93.09	259.1	259.1	509.4	509.4	844.0	844.5	1255.3	1255.5	1753.3	1753.5	2176.9	2327.0
6	15.04	15.05	93.08	93.09	259.1	259.1	509.4	509.3	844.7	844.3	1255.4	1255.4	1753.1	1753.6	2177.8	2327.0
7	15.04	15.04	93.09	93.09	259.0	259.1	509.5	509.5	844.5	844.4	1255.5	1255.6	1753.3	1753.6	2178.2	2326.9
8	15.07	15.07	93.13	93.16	259.0	259.2	509.6	509.7	844.6	844.8	1253.2	1256.0	1753.8	1754.1	2176.7	2328.1
9	15.04	15.04	93.08	93.08	259.1	259.0	509.3	509.4	844.1	844.2	1254.9	1255.1	1753.0	1753.1	2177.7	2326.7
10	15.03	15.04	93.09	93.09	259.0	259.0	509.2	509.3	844.3	844.3	1255.2	1255.1	1753.0	1753.1	2177.7	2326.8
Mean	15.04	15.05	93.09	93.10	259.1	259.1	509.4	509.4	844.3	844.4	1255.0	1255.4	1753.2	1753.4	2177.7	2327.0
RSD (%)	0.08	0.07	0.02	0.02	0.01	0.02	0.02	0.02	0.03	0.02	0.05	0.02	0.01	0.02	0.02	0.02

**Table 5.** Modal damping ratios (in %) of the first eight modes of the cantilever beam determined for different tests from DIC measurements and accelerometers.

Test	Mode 1		Mode 2		Mode 3		Mode 4		Mode 5		Mode 6		Mode 7		Mode 8	
	DIC	Acc.	DIC	Acc.	DIC	Acc.	DIC	Acc.	DIC	Acc.	DIC	Acc.	DIC	Acc.	DIC	Acc.
1	0.45	0.50	0.28	0.28	0.27	0.28	0.15	0.15	0.49	0.49	0.13	0.14	0.14	0.14	0.17	0.15
2	0.46	0.48	0.28	0.28	0.27	0.27	0.15	0.15	0.47	0.49	0.14	0.14	0.13	0.14	0.16	0.15
3	0.47	0.51	0.29	0.28	0.27	0.27	0.15	0.15	0.48	0.49	0.14	0.14	0.13	0.14	0.16	0.15
4	0.45	0.50	0.28	0.28	0.27	0.27	0.16	0.15	0.47	0.48	0.14	0.14	0.13	0.14	0.17	0.16
5	0.48	0.50	0.29	0.28	0.27	0.27	0.14	0.14	0.48	0.50	0.12	0.13	0.13	0.14	0.17	0.15
6	0.49	0.51	0.29	0.28	0.28	0.27	0.16	0.14	0.48	0.50	0.13	0.13	0.14	0.14	0.17	0.15
7	0.49	0.51	0.28	0.28	0.28	0.27	0.15	0.14	0.47	0.50	0.14	0.13	0.14	0.14	0.16	0.15
8	0.55	0.53	0.27	0.25	0.24	0.23	0.13	0.13	0.50	0.51	0.14	0.12	0.14	0.13	0.12	0.14
9	0.47	0.48	0.29	0.28	0.27	0.27	0.16	0.15	0.48	0.49	0.13	0.14	0.14	0.14	0.16	0.15
10	0.47	0.50	0.28	0.28	0.27	0.27	0.16	0.15	0.47	0.49	0.14	0.14	0.14	0.14	0.15	0.15
Mean	0.48	0.50	0.28	0.28	0.27	0.27	0.15	0.14	0.48	0.49	0.13	0.13	0.14	0.14	0.16	0.15
RSD (%)	6.43	3.19	1.86	3.77	3.97	5.14	6.42	4.86	1.96	1.92	5.81	4.22	2.00	1.37	9.01	2.09

### 4.3. Discussion

The major inconvenience of the DIC, compared to other classical instrumentation in dynamics, is the special care taken in the experimental set-up of the tested structure, especially the speckle realization and the lighting, whereas other sensors such as accelerometers and vibrometers are more “ready-to-use”. However, the use of full-field measurements by means of DIC to perform a modal analysis offers many advantages. Given that the surface of the structure under test is not “mechanically” scanned, the duration of the tests is shorter than that needed using scanning vibrometers. As previously underlined, the main advantage of the full-field measurements is the large amount of data points. This amount of data allows us to increase the spatial resolution, leading to a better description of the mode shapes.

Even if the resolution is lower than for accelerometers and vibrometers, we were able to identify using DIC the first six modes of a clamped–clamped beam and the first eight ones of a cantilever beam. The highest natural frequency determined using the full-field measurement here is up to 2200 Hz.

Table 6 summarizes the pros and cons of both measurement techniques considered in this research. We should note that the deviation observed in the identification of the modal damping ratios of some modes with DIC measurements is partially due to the large number of measurement points.

**Table 6.** Comparison between the DIC measurements and accelerometers.

Parameter	DIC		Accelerometers	
Frequency	Good determination	=	Good determination	=
Damping ratio	Some disparity (many measurements)	+ / −	Low disparity (few measurements)	+
Mode shape	Accurate description	+	Lack of points	−
Impact on measurement	Non-intrusive	+	Intrusive	−

## 5. Conclusions

The presented experiments allowed us to demonstrate the feasibility of modal analysis using the displacement measurement with DIC. It must be emphasized that the speckle realization affects the displacement resolution. In the presented investigation, the speckle realized with a pen showed better results in terms of random and systematic errors than that realized with the spray paint. This can be partially explained by the fact that setting



the spot size with a pen is far easier at the scale of the experiment presented in the paper than with spray paint.

The measurement quality realized with DIC has been investigated for the transverse vibratory response of a beam excited by a shock for two boundaries conditions, clamped–clamped and cantilever. To deal with the numerous and noisy signals obtained from the DIC measurements, a continuous wavelet transform method is adapted to perform a modal identification and a signal processing procedure is proposed. The identification was carried out for modes whose frequency goes up to about 2200 Hz, up to the sixth mode for the clamped–clamped beam and the eighth mode for the cantilever beam.

The comparison with the results of modal analysis resulting from the measurement of accelerometers shows that the natural frequencies and the modal damping ratios determined using DIC are very close to those obtained with the accelerometers and that the dispersion of the results is similar. Concerning the mode shapes, the results obtained from DIC measurements are much more accurate due to the large number of points, up to three hundred in our experiments. Thus, one of the interests of using DIC for modal identification of structures is to provide a more accurate description of the mode shapes. This can therefore be very useful for damage detection methods using mode shapes and/or their derivatives, such as modal curvature methods.

**Author Contributions:** Conceptualization, X.R. and G.C.; methodology, G.C.; software, G.C.; validation, G.C.; investigation, X.R.; data curation, G.C.; writing—original draft preparation, X.R.; writing—review and editing, G.C., M.B. and M.Q.; supervision, G.C., M.B. and M.Q.; funding acquisition, G.C., M.B. and M.Q. All authors have read and agreed to the published version of the manuscript.

**Funding:** This work benefited from a grant from the French government managed by the ANR in the framework of the investments of the national program for the future ANR-11-LABX-02-01.

**Institutional Review Board Statement:** Not applicable.

**Informed Consent Statement:** Not applicable.

**Data Availability Statement:** The data are contained within the article.

**Conflicts of Interest:** The authors declare no conflict of interest.

## References

1. Cumunel, G.; Delepine-Lesoille, S.; Argoul, P. Long-gage optical fiber extensometers for dynamic evaluation of structures. *Sens. Actuators A Phys.* **2012**, *184*, 1–15. [[CrossRef](#)]
2. Yang, S.; Allen, M.S. Output-only Modal Analysis using Continuous-Scan Laser Doppler Vibrometry and application to a 20 kW wind turbine. *Mech. Syst. Signal Process.* **2012**, *31*, 228–245. [[CrossRef](#)]
3. Ashory, M.R. Correction of Mass-loading Effects of Transducers and Suspension Effects in Modal Testing. In Proceedings of the 16th International Modal Analysis Conference, Santa Barbara, CA, USA, 2–5 February 1998; Volume 3243, p. 815.
4. Yang, D.S.; Bornert, M.; Chanchole, S.; Gharbi, H.; Valli, P.; Gatmiri, B. Dependence of elastic properties of argillaceous rocks on moisture content investigated with optical full-field strain measurement techniques. *Int. J. Rock Mech. Min. Sci.* **2012**, *53*, 45–55. [[CrossRef](#)]
5. Beberniss, T.; Ehrhardt, D.A. High-speed 3D digital image correlation vibration measurement: Recent advancements and noted limitations. *Mech. Syst. Signal Process.* **2017**, *86 Pt B*, 35–48. [[CrossRef](#)]
6. Reu, P.L.; Rohe, D.P.; Jacobs, L.D. Comparison of {DIC} and {LDV} for practical vibration and modal measurements. *Mech. Syst. Signal Process.* **2017**, *86 Pt B*, 2–16. [[CrossRef](#)]
7. Beberniss, T.; Spottswood, M.; Eason, T. High-Speed Digital Image Correlation Measurements of Random Nonlinear Dynamic Response. In *Experimental and Applied Mechanics*; Proulx, T., Ed.; Springer: New York, NY, USA, 2011; Volume 6, pp. 171–186. [[CrossRef](#)]
8. Siebert, T.; Wood, R.; Splittthof, K. High speed image correlation for vibration analysis. *J. Phys. Conf. Ser.* **2009**, *181*, 012064. [[CrossRef](#)]
9. Wang, W.; Mottershead, J.E.; Siebert, T.; Pipino, A. Frequency response functions of shape features from full-field vibration measurements using digital image correlation. *Mech. Syst. Signal Process.* **2012**, *28*, 333–347. [[CrossRef](#)]
10. Helfrick, M.N.; Niezrecki, C.; Avitabile, P.; Schmidt, T. 3D digital image correlation methods for full-field vibration measurement. *Mech. Syst. Signal Process.* **2011**, *25*, 917–927. [[CrossRef](#)]

11. Hagara, M.; Trebuña, F.; Huňady, R.; Kalina, M.; Schrötter, M. Experimental Identification of Modal Parameters of Thin Metal Sheets by using of DIC. *Proc. Eng.* **2012**, *48*, 180–188. [[CrossRef](#)]
12. Wang, W.; Mottershead, J.E.; Ihle, A.; Siebert, T.; Reinhard Schubach, H. Finite element model updating from full-field vibration measurement using digital image correlation. *J. Sound Vib.* **2011**, *330*, 1599–1620. [[CrossRef](#)]
13. Chen, J.G.; Wadhwa, N.; Cha, Y.J.; Durand, F.; Freeman, W.T.; Buyukozturk, O. Modal identification of simple structures with high-speed video using motion magnification. *J. Sound Vib.* **2015**, *345*, 58–71. [[CrossRef](#)]
14. Bornert, M.; Brémand, F.; Doumalin, P.; Dupré, J.C.; Fazzini, M.; Grédiac, M.; Hild, F.; Mistou, S.; Molimard, J.; Orteu, J.J.; et al. Assessment of Digital Image Correlation Measurement Errors: Methodology and Results. *Exp. Mech.* **2008**, *49*, 353–370. [[CrossRef](#)]
15. Bornert, M.; Vales, F.; Gharbi, H.; Nguyen Minh, D. Multiscale full-field strain measurements for micromechanical investigations of the hydromechanical behaviour of clayey rocks. *Strain* **2010**, *46*, 33–46. [[CrossRef](#)]
16. Dautriat, J.; Bornert, M.; Gland, N.; Dimanov, A.; Raphanel, J. Localized deformation induced by heterogeneities in porous carbonate analysed by multi-scale digital image correlation. *Tectonophysics* **2011**, *503*, 100–116. [[CrossRef](#)]
17. Martin, G.; Caldemaison, D.; Bornert, M.; Pinna, C.; Bréchet, Y.; Véron, M.; Mithieux, J.D.; Pardoën, T. Characterization of the High Temperature Strain Partitioning in Duplex Steels. *Exp. Mech.* **2013**, *53*, 205–215. [[CrossRef](#)]
18. Bornert, M.; Orteu, J.J.; Roux, S. Corrélation d'images. In *Mesures de Champs et Identification en Mécanique des Solides*; Grédiac, M., Hild, F., Eds.; *Traité MIM, Série Matériaux et Métallurgie*; Hermes Science Publications Lavoisier: Paris, France, 2011; Chapter 6, pp. 175–208.
19. Doumalin, P.; Bornert, M. Micromechanical applications of digital image correlation techniques. In *Interferometry in Speckle Light*; Springer: Berlin/Heidelberg, Germany, 2000; Volume 3243, pp. 67–74. [[CrossRef](#)]
20. Lecompte, D.; Smits, A.; Bossuyt, S.; Sol, H.; Vantomme, J.; Van Hemelrijck, D.; Habraken, A.M. Quality assessment of speckle patterns for digital image correlation. *Opt. Lasers Eng.* **2006**, *44*, 1132–1145. [[CrossRef](#)]
21. Crammond, G.; Boyd, S.W.; Dulieu-Barton, J.M. Speckle pattern quality assessment for digital image correlation. *Opt. Lasers Eng.* **2013**, *51*, 1368–1378. [[CrossRef](#)]
22. Bossuyt, S. Optimized Patterns for Digital Image Correlation. In *Imaging Methods for Novel Materials and Challenging Applications*; Jin, H., Sciammarella, C., Furlong, C., Yoshida, S., Eds.; Springer: New York, NY, USA, 2013; Volume 3, pp. 239–248. [[CrossRef](#)]
23. Amiot, F.; Bornert, M.; Doumalin, P.; Dupré, J.C.; Fazzini, M.; Orteu, J.J.; Poilâne, C.; Robert, L.; Rotinat, R.; Toussaint, E.; et al. Assessment of Digital Image Correlation Measurement Accuracy in the Ultimate Error Regime: Main Results of a Collaborative Benchmark: Benchmark on Digital Image Correlation Ultimate Error. *Strain* **2013**, *49*, 483–496. [[CrossRef](#)]
24. Géradin, M.; Rixen, D. *Mechanical Vibrations: Theory and Application to Structural Dynamics*; Wiley: Hoboken, NJ, USA, 1997.
25. Le, T.P.; Argoul, P. Continuous wavelet transform for modal identification using free decay response. *J. Sound Vib.* **2004**, *277*, 73–100. [[CrossRef](#)]
26. Le, T.P.; Paultre, P. Modal identification based on continuous wavelet transform and ambient excitation tests. *J. Sound Vib.* **2012**, *331*, 2023–2037. [[CrossRef](#)]
27. Allemang, R.J.; Brown, D.L. A correlation coefficient for modal vector analysis. In *Proceedings of the 1st International Modal Analysis Conference, SEM, Orlando, FL, USA, 8–10 November 1982*; Volume 1, pp. 110–116.

**Disclaimer/Publisher's Note:** The statements, opinions and data contained in all publications are solely those of the individual author(s) and contributor(s) and not of MDPI and/or the editor(s). MDPI and/or the editor(s) disclaim responsibility for any injury to people or property resulting from any ideas, methods, instructions or products referred to in the content.